Available online at www.sciencedirect.com
SCIENCE DIRECT®
Journal of Computational Physics 201 (2004) 397–420
JOURNAL OF COMPUTATIONAL PHYSICS
www.elsevier.com/locate/jcp

On a numerical strategy to compute gravity currents of non-Newtonian fluids

D. Vola *, F. Babik, J.-C. Latché

Direction de la Prévention des Accidents Majeurs, Institut de Radioprotection et de Sûreté Nucléaire (IRSN), BP3-13115 St. Paul-lez-Durance Cedex, France

Received 20 October 2003; received in revised form 15 March 2004; accepted 28 May 2004
Available online 6 July 2004

Abstract

This paper is devoted to the presentation of a numerical scheme for the simulation of gravity currents of non-Newtonian fluids. The two dimensional computational grid is fixed and the free-surface is described as a polygonal interface independent from the grid and advanced in time by a Lagrangian technique. Navier–Stokes equations are semi-discretized in time by the Characteristic-Galerkin method, which finally leads to solve a generalized Stokes problem posed on a physical domain limited by the free surface to only a part of the computational grid. To this purpose, we implement a Galerkin technique with a particular approximation space, defined as the restriction to the fluid domain of functions of a finite element space. The decomposition–coordination method allows to deal without any regularization with a variety of non-linear and possibly non-differentiable constitutive laws. Beside more analytical tests, we revisit with this numerical method some simulations of gravity currents of the literature, up to now investigated within the simplified thin-flow approximation framework.

Keywords: Free surface flows; Viscoplastic fluids; Herschel–Bulkley model; Fictitious node FEM; Characteristics/Galerkin method; Decomposition–coordination method; Gravity currents

1. Introduction

Free-surface flows are involved in a wide range of phenomena, including both natural hazards (mud or lava flows for instance) and industrial applications (mould filling, to give just one example). In the context of nuclear safety, we are faced to the challenge of simulating high temperature flows of fluids with complex constitutive laws, cooled by radiative heat transfer at the free surface. The numerical method we present here has been designed to cope with this problem and widely used at the Institut de Radioprotection et de Sûreté Nucléaire (IRSN) within the last decade. A dedicated software, namely the CROCO code, has been

* Corresponding author. Tel.: +33-4-4225-6350; fax: +33-4-4225-6143.
E-mail address: didier.vola@irsn.fr (D. Vola).

0021-9991/$ - see front matter
doi:10.1016/j.jcp.2004.05.019

developed and compared to numerous experimental results [25,28]. Basically, our objective here is to develop a numerical scheme for free surface flows meeting the following requirements: first, for the purpose of simplicity of implementation, working with a fixed meshing, second, being able to capture steep gradients at the free surface, finally, dealing with a wide range of constitutive laws for the fluid, including the viscoplastic ones. The first two items have motivated the development of a specific numerical scheme, combining the standard characteristic-Galerkin time splitting strategy with a non-standard spatial discretization. The last requirement is fulfilled by making use of the so-called "decomposition–coordination" method. After a formulation of the governing equations of the problem under consideration, we detail successively these two points in Sections 3 and 4. The last part of the paper is devoted to numerical tests, to assess the capabilities of the presented numerical scheme. To this purpose, we revisit in particular two test problems consisting in the simulation of two-dimensional isothermal non-Newtonian gravity currents, already studied in the literature within the so-called thin flow approximation framework. Practical situations addressed in this paper are two-dimensional, and the exposition is restricted to this case; however, the transposition to the three-dimensional case of most of the ideas presented here is straightforward.

2. Governing equations

We are interested in this paper in generalized Newtonian fluids [4], i.e., in fluids the behavior of which is modeled by a viscosity that, in contrast to the Newtonian model, varies with the shear strain rate tensor $D = 1/2(\nabla u + \nabla^t u)$. Using both physical and mathematical arguments, the viscosity is classically shown for incompressible flows to depend only on the second principal invariant $|D|$ of D with

$$|D| = \sqrt{D : D} = \sqrt{\sum_{i,j} D_{ij} D_{ij}}.$$

The rest of the nomenclature is presented in Table 1. Classical formulation for the constitutive law of those generalized Newtonian fluids is the following one:

$$\tau = \mu(|D|)D. \tag{1}$$

Viscoplastic fluids may also be considered to fall in this class of models but, due to the presence of a yield stress in the constitutive law, the formulation (1) turns to a multi-valued expression in the so-called "unsheared" or "solid" zones of the flow where the shear strain rate vanishes and the apparent viscosity becomes infinite.

In fact, the thermodynamic of irreversible isothermal processes together with some results of convex analysis allows to set a more suitable framework to model standard generalized Newtonian fluids, including viscoplastic ones. Fluids we will consider here are those ones for which there exists a convex, lower-semicontinuous, positive and minimal at zero functional ψ (a thermodynamical pseudo-potential) such that the constitutive law can be expressed as the generalized equation [12]

Table 1
Nomenclature for the constitutive relations

u	Velocity field	μ	Consistency
σ	Cauchy stress tensor	ρ	Density
p	Pressure field	τ_Y	Plasticity threshold
τ	Shear stress tensor	N	Exponent
ψ	Internal dissipation potential	g	Gravity field

$$\tau = \sigma + pI \in \partial_{\mathrm{D}}\psi. \tag{2}$$

where $\partial_{\mathrm{D}}\psi$ stands for the subdifferential of ψ. The constitutive law is now determined by the expression of this internal dissipation pseudo-potential that is again assumed to depend only on $|D|$. This class of materials is generally qualified as fluids presenting a "standard generalized behavior". We give on the left column of Table 2 the expressions of the dissipation pseudo-potential ψ for some classical rheological models we will use in this publication, i.e., the Herschel–Bulkley model and its two limit cases, the Bingham model and the Power-Law model, but other classical rheological models such as Casson model also enters this framework. The equivalent relations given on the right column of Table 2 can be derived at least formally from the constitutive law as defined by (2) and the expression of ψ, by using the characterization of the sub-differential $\partial_{\mathrm{D}}\psi$

$$\forall E \quad \psi(E) - \psi(D) \geqslant \tau : (E - D). \tag{3}$$

From our point of view, the main interest of those developed forms of the constitutive law is to highlight, for fluid concerned by a yield stress, the implicit splitting of the fluid domain into its "flow" and "no-flow" parts.

The fluid domain Ω_{f} (boundary $\partial\Omega_{\mathrm{f}}$), i.e., the volume occupied by the fluid is assumed at any time t of the time interval $]0, T]$ to lie within a fixed computational domain Ω which is a polygonal open and bounded subset of the physical space. We denote by χ_{f} the characteristic function of the fluid domain Ω_{f} on Ω (identically one in Ω_{f} and zero elsewhere). The fluid motion is governed by the Navier–Stokes set of equations over a variable domain:

$$\text{Find for all } t \in]0, T] \quad \left| \begin{array}{l} \text{the fluid domain } \Omega_{\mathrm{f}}(t) = \{x \in \Omega \text{ s.t. } \chi_{\mathrm{f}}(x) = 1\}, \\ \text{the velocity field } u(\cdot, t), \end{array} \right.$$

such that:

$$\begin{cases} \dfrac{\partial \chi_{\mathrm{f}}}{\partial t} + u \cdot \nabla \chi_{\mathrm{f}} = 0, \\ \rho\left(\dfrac{\partial u}{\partial t} + (u \cdot \nabla)u \right) - \nabla \cdot \sigma = \rho g, \\ \nabla \cdot u = 0, \\ \sigma + pI \in \partial_{\mathrm{D}}\psi, \end{cases} \tag{4}$$

together with boundary conditions over $\partial\Omega_{\mathrm{f}}$ and initial conditions $\Omega_{\mathrm{f}}(0) \subset \Omega$ and $u(\cdot, 0)$.

As soon as the last relation of this system, defining the fluid rheological properties, cannot be exploited to derive an one-to-one expression of the shear stress tensor of the form of Eq. (1), i.e., for cases under consideration here, for viscoplastic fluids, the momentum balance equation must be understood in some weak sense (see e.g. [9] for an in-depth discussion on this topic).

Table 2
Constitutive laws

Herschel–Bulkley	
$\psi(D) = \frac{2\mu}{N+1}\lvert D\rvert^{N+1} + \tau_{\mathrm{Y}}\lvert D\rvert$	$\lvert\tau\rvert \leqslant \tau_{\mathrm{Y}} \Longleftrightarrow D = 0,$ $\lvert\tau\rvert > \tau_{\mathrm{Y}} \Longleftrightarrow \tau = (\frac{\tau_{\mathrm{Y}}}{\lvert D\rvert} + 2\mu\lvert D\rvert^{N-1})D$
Bingham	
$\psi(D) = \mu\lvert D\rvert^2 + \tau_{\mathrm{Y}}\lvert D\rvert$	$\lvert\tau\rvert \leqslant \tau_{\mathrm{Y}} \Longleftrightarrow D = 0,$ $\lvert\tau\rvert > \tau_{\mathrm{Y}} \Longleftrightarrow \tau = (\frac{\tau_{\mathrm{Y}}}{\lvert D\rvert} + 2\mu)D$
Power-Law	
$\psi(D) = \frac{2\mu}{N+1}\lvert D\rvert^{N+1}$	$\tau = 2\mu\lvert D\rvert^{N-1}D$

3. Solving moving boundaries problem: the fictitious degrees of freedom method

Many solution methods have been developed in the last decades for modeling flows with interfaces making use of Eulerian discretizations and some reviews can be found in the literature, see a.o. [20,29] and references herein. By contrast to all those methods for which the interface is "captured" by analyzing any characteristic function such as VOF methods [19], level set methods [26,32] or phase field methods [17,18], the strategy we employ leads to track directly the interface, which representation is completely independent from the computational grid used to solve the flow balance equation. This method is general, in the sense that it can be used to solve Navier–Stokes equation as well as, for instance, transport (convection–diffusion) equations in the fluid, provided of course the velocity field is known. This is why we have chosen to present it in a dedicated section. It makes use of three basic ingredients, which can be presented as an answer to respectively the three following problems: describing the free surface and computing its motion, discretizing in time a partial differential equation (PDE) posed on a moving spatial domain, solving a PDE on a subdomain of the computational domain with a general (i.e., independent from the spatial discretization) boundary. This three items are successively addressed in this section. The first two ones will probably appear to the reader as nowadays well-known numerical recipes; they are however reasonably detailed for the sake of completeness. The time interval $]0,T]$ is divided into subintervals $]t^n,t^{n+1}]$ assumed for the sake of readability to be of equal length δt. We suppose given a quasi-uniform triangulation $\mathscr{T}_h$ [7] of the computational domain Ω; it will be referred to in the following as the computational grid. The parameter h is defined as $h=\sup_{K\in\mathscr{T}_h}(h_K)$ where h_K denotes the diameter of the smallest circle including the polyhedron K.

3.1. Free surface motion

The free surface is described by a polygon whose vertex positions X_s are independent from the computational grid and are submitted to the following Lagrangian evolution equation:

$$\frac{\mathrm{d}X_s}{\mathrm{d}t}=u(X_s). \tag{5}$$

This latter is discretized using the forward Euler method in

$$X_s^{n+1}=X_s^n+\delta t\,u^n(X_s^n). \tag{6}$$

This method is rather simplistic and can be enriched in the following directions. First of all, as all other interface tracking methods, it does not address naturally the merging or tearing phenomena. Moreover, no artificial interfacial viscosity is introduced, which is an advantage in terms of accuracy but, on the opposite, a drawback concerning the computational reliability. Finally, one may need to adopt some strategies to cope with some boundary effects: mainly, in the particular context of gravity currents, for setting the height of the free surface in the entrance section and for the description of the flow front. This is the main difficulty to overcome for the transposition of the two-dimensional scheme presented here to the three-dimensional case.

In our algorithm, the Lagrangian transport of the free surface, defining the new fluid domain boundaries, is the first stage of the time step.

3.2. Semi-discretization of the balance equations by the transport-Galerkin method

When performing the time discretization on an Eulerian mesh of an unstationary balance equation posed over a moving boundary domain, any method based on some truncation of Taylor developments must

come with a reconstruction method of the unknown field values at some previous times at nodes of the new fluid domain as shown in Fig. 1. Coming back to a Lagrangian description to the fluid motion is a natural way to avoid such a complex reconstruction of the unknown fields. The trajectory curve (the characteristic ξ_x^{n+1}, see a.o. [3,14]) of the fluid particle that will be at position x at time t^{n+1} is solution of the final value ODE

$$\begin{cases} \dfrac{\mathrm{d}\xi_x^{n+1}(t)}{\mathrm{d}t} = u^n(\xi_x^{n+1}(t)) & \forall t \in [t^n, t^{n+1}], \\ \xi_x^{n+1}(t^{n+1}) = x, \end{cases}$$

which is is approximated at the first order by $\xi^* : [t^n, t^{n+1}] \to \mathbb{R}^2$:

$$\xi^*(t) + (t^{n+1} - t)u^n(\xi^*(t)) = x.$$

Then the method of characteristics leads to an approximation of the material derivative of u (here to the first order)

$$\frac{\mathrm{d}u}{\mathrm{d}t}(x, t^{n+1}) \approx \frac{u^{n+1}(x) - u^n(\xi^*(t^n))}{\delta t}.$$

As an other advantage of this Lagrangian approximation method, in opposite to standard methods leading to an approximation of the local derivative, it overcomes directly numerical difficulties due to the non-symmetry of the convective operator $(u.\nabla\cdot)u$ and the efficiency of the finite element method for symmetrical differential operators is retrieved.

3.3. Spatial discretization: the fictitious degrees of freedom method

Finally, the problem we then have to solve at each time step is a second order elliptic system, here a generalized Stokes problem, posed over a new fixed domain Ω_f^{n+1}. To this purpose, the general form of a Galerkin method for the momentum balance equation, for instance, reads:

$$\begin{aligned} &\text{Find } u^{n+1} \in \mathscr{U}^{n+1} \quad \text{such that } \forall v \in \mathscr{V}, \\ &\int_{\Omega_f^{n+1}} \rho \frac{u^{n+1}(x)}{\delta t}.v \,\mathrm{d}\Omega - \int_{\Omega_f^{n+1}} \nabla \cdot \sigma^{n+1}.v \,\mathrm{d}\Omega = \int_{\Omega_f^{n+1}} f.v \,\mathrm{d}\Omega, \end{aligned} \tag{7}$$

where $\mathscr{U}^{n+1}$ and $\mathscr{V}$ are subspaces of the Sobolev space $[\mathscr{H}^1(\Omega_f^{n+1})]^2$ to be defined according to the boundary conditions of the problem. As the fluid domain interface representation is strictly disconnected from the

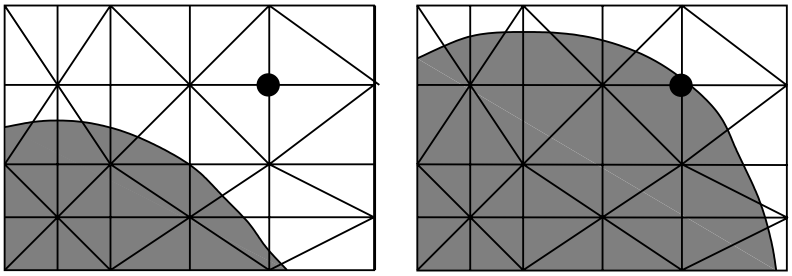

Fig. 1. Computational grid and fluid domain at time t^n and t^{n+1}. Unknowns fields must be reconstructed at node marked by a bullet for all previous times needed by the time discretization method.

computational grid $\mathscr{T}_h$, the construction of an approximation space for $\mathscr{U}^{n+1}$ and $\mathscr{V}$, together with the associated quadrature rules for a (possibly exact) integration over Ω_f^{n+1}, is far from standard. This is the topic of the rest of the section.

Among all polyhedra of $\mathscr{T}_h$, we exclude those that do not intersect Ω_f^{n+1}. We will qualify hereafter a polyhedron that lies entirely on Ω_f^{n+1} as "filled" polyhedron and a polyhedron that has a partial intersection with Ω_f^{n+1} as "partially filled" polyhedron, see Fig. 2.

Over "filled" polyhedra, we choose a standard finite element approximation. Over "partially filled" polyhedra, we keep the space spanned by the same shape functions or, in other words, we choose as approximation space the restriction to the fluid domain of the standard finite element space under consideration. This procedure leads to make use of fictitious nodes, i.e., to consider nodes that will be associated to discrete unknowns for the problem even if they are located outside the fluid domain (nodes 2 and 3 on right side of Fig. 2). These "fictitious degrees of freedom" have no other meaning than being involved in the development of the unknown fields over $K \cap \Omega_f^{n+1}$. The obtained discrete space provides an internal approximation of $\mathscr{U}^{n+1}$ and $\mathscr{V}$ whenever no Dirichlet boundary condition is to be imposed on the immersed boundary of the fluid domain. In the opposite case, Dirichlet conditions must be imposed in some weak sense (by penalization or using Lagrange multipliers), see Section 5.1 for a practical example.

Over filled polyhedra, standard quadrature rules may be employed (see the left side of Fig. 3 for a third-order rule). To build same order quadrature rules over a "partially filled" polyhedron K, we proceed as follows. The polygonal domain $K \cap \Omega_f^{n+1}$ is first triangulated. The specific quadrature rule on $K \cap \Omega_f^{n+1}$ is then obtained by addition of the standard quadrature rules on each generated triangle, see Fig. 3. No geometrical aspect property is required for triangles issued from the triangulation process, contrary to those of the computational grid, and any fast triangulation algorithm such as the "cut-an-ear" algorithm [34] can be used.

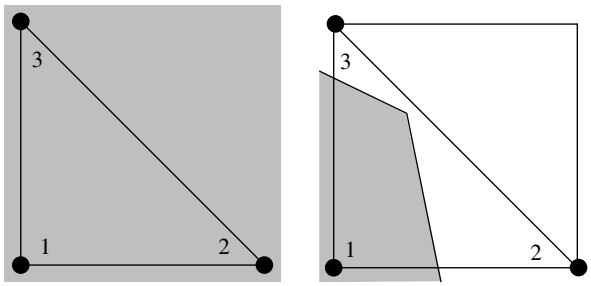

Fig. 2. "Filled" and "partially filled" triangle.

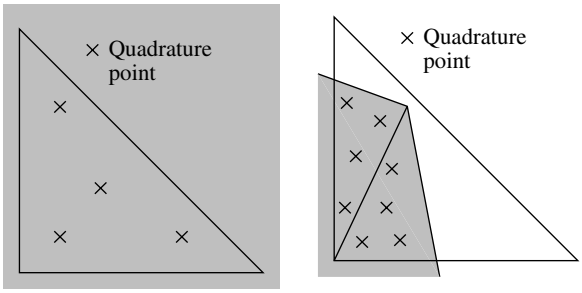

Fig. 3. Example of quadrature rules for a "filled" and "partially filled" triangle.

Defining a generalized Clement interpolation operator, it is shown in [21] that, under mild regularity conditions for the free surface, the non-standard finite element space built here provides an approximation of the same order as standard finite element discretizations, i.e., using "fitted-to-the-physical-domain" grids. In particular, the same accuracy is kept up to the immersed boundary. This fact is also checked by numerical experiments described in [21] and by the test presented in Section 5.1.

From a practical point of view, one only needs with this numerical scheme to make use of special quadrature rules for the algebraic problem assembling. When using object-oriented designed software, it is then possible to "isolate" the responsibility of providing integration rules for a given polyhedron in such a way that how the integration is performed is hidden for the assembling process and any FE solver designed to a "fitted-to-the-physical-domain" grid can be directly reused. This is the case for the software used here, namely the CROCO code based on the software component library PELICANS, both developed at IRSN by our team.

3.4. Overall algorithm

Finally, the numerical scheme presented here can be viewed as a time splitting scheme as summed-up in Table 3. The convected velocity $u^*(x)$ is used to build the explicit part of inertial term and has to be evaluated at the points of the quadrature rules.

4. Solving the generalized stokes problem for quasi-Newtonian fluids

Our purpose in this section is to design a numerical strategy to cope with the wide range of constitutive models presented in Section 2 without any regularization, even in presence of yield stress. This strategy is based on the seminal works of Duvaut and Lions [9] and Fortin and Glowinsky [11,13, Chapter III and VI of respectively] and has already been presented in case of the Bingham model in [35] (see also e.g. [8,30] for related works). It is essentially summed-up here, with a special emphasis on how it can be extended to the whole class of constitutive models under consideration. In this section, for readability's sake, exponents referred to time step will be omitted. Using classical results for variational inequalities of the second kind [9] and the definition of the subdifferential, one can give a formally equivalent form of the generalized Stokes problem (7), find $u \in \{v \in \mathscr{V} | \nabla \cdot v = 0\}$ such that

$$\mathscr{G}(u) + \mathscr{F}(D(u)) = \min_{v} [\mathscr{G}(v) + \mathscr{F}(D(v))],$$

where the terms due to the constitutive law are separated from inertial and external forces terms:

$$\mathscr{G}(v) = \frac{\rho}{2\delta t} \int_{\Omega_f} v.v \, d\Omega - \int_{\Omega_f} f.v \, d\Omega \quad \text{and} \quad \mathscr{F}(D(v)) = \int_{\Omega_f} \psi(D(v)) \, d\Omega.$$

In functional $\mathscr{F}$, ψ represents the internal dissipation potential of Section 2.

Table 3
Time splitting numerical scheme

From time t^n to time t^{n+1}
⇒ Convective step:
- Free surface transport independent of the computational grid $\Omega_f(t^n) \xrightarrow{u^n} \Omega_f(t^{n+1})$,
- Quadrature rules on "partially filled" polyhedra,
- Determination of the "convected velocity" by the method of characteristics for all $x \in \Omega_f(t^{n+1})$, find $u^*(x) = u^n(\xi^*(t^n))$.

⇒ Diffusive step:
generalized Stokes problem (7) on $\Omega_f(t^{n+1})$

An auxiliary primal variable γ representing the shear strain rate $D(u)$ is then introduced (decomposition step). Now one has to find

$$(u,\gamma) \in \{(v,w) \in \mathscr{V} \times \mathscr{W} | \nabla \cdot v = 0, w = D(v)\} \quad \text{such that}: \ \mathscr{G}(u) + \mathscr{F}(\gamma) = \min_{(v,w)} [\mathscr{G}(v) + \mathscr{F}(w)],$$

where the space $\mathscr{W} = [\mathscr{L}^2(\Omega)]^4$. The constraints $\nabla \cdot (u) = 0$ and $\gamma = D(u)$ are relaxed by introducing two Lagrange multipliers p and λ homogeneous to a pressure and to a shear stress, respectively (coordination step), leading to the following saddle point problem, find $(u,\gamma,p,\lambda) \in \mathscr{V} \times \mathscr{W} \times \mathscr{Q} \times \mathscr{W}$ such that:

$$\mathscr{L}_{\mathrm{r}}(u,\gamma,p,\lambda) = \inf_{(v,w)\in\mathscr{V}\times\mathscr{W}} \left(\sup_{(q,v)\in\mathscr{Q}\times\mathscr{W}} \mathscr{L}_{\mathrm{r}}(v,w,q,v) \right), \tag{8}$$

where $\mathscr{L}_{\mathrm{r}}$ stands for the augmented Lagrangian functional defined on $\mathscr{V} \times \mathscr{W} \times \mathscr{Q} \times \mathscr{W}$ by

$$\mathscr{L}_{\mathrm{r}}(v,w,q,v) = \mathscr{G}(v) + \mathscr{F}(w) - \langle v, w - D(v)\rangle_{\mathscr{W}} - \langle \nabla \cdot v, q\rangle_{\mathscr{Q}} + \frac{r_1}{2}||w - D(v)||^2_{\mathscr{W}} + \frac{r_2}{2}||\nabla \cdot v||^2_{\mathscr{Q}},$$

where $\mathscr{Q} = \mathscr{L}^2_0(\Omega)$ and r_1, r_2 are two penalty parameters.

We associate to each polyhedron K of the triangulation $\mathscr{T}_{\mathrm{h}}$ three Lagrange finite elements to build discrete sets of admissible velocities, pressures and additional variables:

$$\begin{aligned}
\mathscr{V}_{\mathrm{h}} &= [\mathscr{X}_{\mathrm{h}}]^2 = \left[\left\{ v_i \in \mathscr{C}^0(\bar{\Omega}) \quad \text{such that } v_i|K \in \varphi_K \quad \forall K \in \mathscr{T}_{\mathrm{h}} \right\} \right]^2 \subset \mathscr{V}, \\
\mathscr{Q}_{\mathrm{h}} &= \left\{ q \in \mathscr{L}^2(\bar{\Omega}) \quad \text{such that } q_{|K} \in \pi_K \quad \forall K \in \mathscr{T}_{\mathrm{h}} \right\} \subset \mathscr{Q}, \\
\mathscr{W}_{\mathrm{h}} &= \left[\left\{ w_{i,j} \in \mathscr{L}^2(\bar{\Omega}) \quad \text{such that } w_{i,j}|K \in \psi_K \quad \forall K \in \mathscr{T}_{\mathrm{h}} \right\} \right]^{2\times 2} \subset \mathscr{W},
\end{aligned}$$

where φ_K and π_K are assumed to be the sets of linear functions on K whereas ψ_K is assumed to be the set of constant functions over K.

This association of such equal order approximation spaces for the velocity field and the pressure field does not fulfill the Brezzi–Babuska stability condition for the standard velocity/pressure linear Stokes mixed problem. This can be circumvented using the Brezzi–Pitkäranta non consistent stabilization method [6].

Remark 1. Note that consistent methods such as GLS or PSPG methods cannot be directly extended to the problem at hand. Indeed, they are based on a "strong" formulation of the form of Eq. (4), and such a relation does not hold for fluids exhibiting a yield stress. Use of consistent stabilization methods then seems to force to regularize in some sense the problem. As an example, Perić and Slijepčević [27] have used the GLS stabilization method for a regularized problem based on the Panastasiou's model for viscoplastic fluids.

We have checked for a class of abstract mixed problems including Stokes problem for Bingham fluids that the Brezzi–Pitkäranta stabilization technique leads to a stable discretization and that the perturbation introduced does not change significantly the error estimates [22].

We search now for $(u_{\mathrm{h}},\gamma_{\mathrm{h}},p_{\mathrm{h}},\lambda_{\mathrm{h}}) \in \mathscr{V}_{\mathrm{h}} \times \mathscr{W}_{\mathrm{h}} \times \mathscr{Q}_{\mathrm{h}} \times \mathscr{W}_{\mathrm{h}}$ such that

$$\mathscr{L}_{\mathrm{h}}(u_{\mathrm{h}},\gamma_{\mathrm{h}},p_{\mathrm{h}},\lambda_{\mathrm{h}}) = \inf_{(v_{\mathrm{h}},w_{\mathrm{h}})\in\mathscr{V}_{\mathrm{h}}\times\mathscr{W}_{\mathrm{h}}} \left(\sup_{(q_{\mathrm{h}},v_{\mathrm{h}})\in\mathscr{Q}_{\mathrm{h}}\times\mathscr{W}_{\mathrm{h}}} \mathscr{L}_{\mathrm{h}}(v_{\mathrm{h}},w_{\mathrm{h}},q_{\mathrm{h}},v_{\mathrm{h}}) \right), \tag{9}$$

where $\mathscr{L}_{\mathrm{h}}$ stands for the augmented Lagrangian functional defined on $\mathscr{V}_{\mathrm{h}} \times \mathscr{W}_{\mathrm{h}} \times \mathscr{Q}_{\mathrm{h}} \times \mathscr{W}_{\mathrm{h}}$ by

$$\mathscr{L}_{\mathrm{h}}(v_{\mathrm{h}}, w_{\mathrm{h}}, q_{\mathrm{h}}, \nu_{\mathrm{h}}) = \mathscr{G}(v_{\mathrm{h}}) + \mathscr{F}(w_{\mathrm{h}}) - \langle \nu_{\mathrm{h}}, w_{\mathrm{h}} - D(v_{\mathrm{h}})\rangle_{\mathscr{W}} - \langle \nabla \cdot v_{\mathrm{h}}, q_{\mathrm{h}}\rangle_{\mathscr{Q}} + \frac{r_1}{2}||w_{\mathrm{h}} - D(v_{\mathrm{h}})||^2_{\mathscr{W}} + \frac{r_2}{2}||\nabla \cdot v_{\mathrm{h}}||^2_{\mathscr{Q}} - \frac{\alpha}{2}\sum_{K\in\mathscr{T}_{\mathrm{h}}} h_K^2 ||\nabla q_{\mathrm{h}}||^2_K$$

and where the last term in this Lagrangian functional corresponds to the Brezzi–Pitkäranta perturbation.

The problem is solved using a variant of the fully decoupled algorithm ALG2 of [11,13] which can be viewed as an Uzawa method with a staggered update of the primal variables, see Table 4. The algorithm is proven to be convergent provided that the following relations between descent and augmentation parameters hold [22]:

$$\rho_1 \leqslant \frac{1+\sqrt{5}}{2} r_1 \quad \text{and} \qquad \rho_2 \leqslant 2 r_2.$$

As $\mathscr{W}_{\mathrm{h}}$ is the set of piecewise constant tensors on $\mathscr{T}_{\mathrm{h}}$, one easily checks that the optimality condition associated to γ (second step of the algorithm) turns to the following series of scalar minimization problems, for all $K \in \mathscr{T}_{\mathrm{h}}$ find γ_K^l such that:

$$\gamma_K^l = \frac{\gamma_{\mathrm{h}}^*}{||\beta_K||}\beta_K,$$

where $\beta_K = \lambda_K^{l-1} + \frac{r_1}{\int_K \mathrm{d}\Omega}\int_K D(u_{\mathrm{h}}^l)\,\mathrm{d}\Omega$ and γ_{h}^* is the solution of:

$$\begin{cases} \theta(\gamma_{\mathrm{h}}^*) = \min_{z\in\mathbb{R}} \theta(z), \\ \theta(z) = \left[\psi(z) + \frac{r_1}{2}(z)^2 - ||\beta_K||z\right]. \end{cases} \tag{10}$$

The solution of each of those minimization problem (10) depends on the constitutive law. As an example, in case of the Herschel–Bulkley model, it can be developed to yield, for all $K \in \mathscr{T}_{\mathrm{h}}$:

$$\begin{cases} ||\beta_K|| \leqslant \tau_{\mathrm{Y}} & \Longleftrightarrow \quad ||\gamma_K^l|| = 0, \\ ||\beta_K|| > \tau_{\mathrm{Y}} & \Longleftrightarrow \quad \psi'(||\gamma_K^l||) + r_1||\gamma_K^l|| - ||\beta_K|| = 0, \end{cases}$$

where the singularity for vanishing shear strain rate magnitude has been circumvented. The non-linear equation corresponding to the sheared zones ($||\beta_K|| > \tau_{\mathrm{Y}}$) admits an explicit solution in case of Bingham fluids, see [10,35] and can be solved in the Herschel–Bulkley case using the Newton method or any of its variants. In the quite general case, one has to solve the scalar minimization problem (10) of a convex, semi-continuous and positive functional and many methods have been developed since the nineties to this particular aim, see a.o. [24].

Table 4
Algorithm for the diffusive step

$(u_{\mathrm{h}}^{l-1}, \gamma_{\mathrm{h}}^{l-1}, p_{\mathrm{h}}^{l-1}, \lambda_{\mathrm{h}}^{l-1})$ being known, find $(u_{\mathrm{h}}^l, \gamma_{\mathrm{h}}^l, p_{\mathrm{h}}^l, \lambda_{\mathrm{h}}^l)$ solving the following four steps successively
$\forall (v_{\mathrm{h}}, w_{\mathrm{h}}, q_{\mathrm{h}}, \nu_{\mathrm{h}}) \in \mathscr{V}_{\mathrm{h}} \times \mathscr{W}_{\mathrm{h}} \times \mathscr{Q}_{\mathrm{h}} \times \mathscr{W}_{\mathrm{h}}$:

- $\langle \mathscr{G}'(u_{\mathrm{h}}^l); v_{\mathrm{h}} - u_{\mathrm{h}}^l\rangle_{\mathscr{V}_{\mathrm{h}}} - \langle p_{\mathrm{h}}^{l-1}; \nabla\cdot(v_{\mathrm{h}} - u_{\mathrm{h}}^l)\rangle_{\mathscr{Q}_{\mathrm{h}}} + \langle \lambda_{\mathrm{h}}^{l-1}; \nabla(v_{\mathrm{h}} - u_{\mathrm{h}}^l)\rangle_{\mathscr{W}_{\mathrm{h}}}$
  $+ r_1\langle \nabla u_{\mathrm{h}}^l - \gamma_{\mathrm{h}}^{l-1}; \nabla(v_{\mathrm{h}} - u_{\mathrm{h}}^l)\rangle_{\mathscr{W}_{\mathrm{h}}} + r_2\langle \nabla\cdot u_{\mathrm{h}}^l; \nabla\cdot(v_{\mathrm{h}} - u_{\mathrm{h}}^l)\rangle_{\mathscr{Q}_{\mathrm{h}}} \geqslant 0$
- $\mathscr{F}(w_{\mathrm{h}}) - \mathscr{F}(\gamma_{\mathrm{h}}^l) - \langle \lambda_{\mathrm{h}}^{l-1}; w_{\mathrm{h}} - \gamma_{\mathrm{h}}^l\rangle_{\mathscr{W}_{\mathrm{h}}} + r_1\langle w_{\mathrm{h}} - \nabla u_{\mathrm{h}}^l; w_{\mathrm{h}} - \gamma_{\mathrm{h}}^l\rangle_{\mathscr{W}_{\mathrm{h}}} \geqslant 0$
- $\langle p_{\mathrm{h}}^l - p_{\mathrm{h}}^{l-1}; q_{\mathrm{h}}\rangle_{\mathscr{Q}_{\mathrm{h}}} = -\rho_1\left[\langle \nabla\cdot u_{\mathrm{h}}^l; q_{\mathrm{h}}\rangle_{\mathscr{Q}_{\mathrm{h}}} + \alpha\sum_{K\in\mathscr{T}_{\mathrm{h}}} h_K^2\langle \nabla p_{\mathrm{h}}^l; \nabla q_{\mathrm{h}}\rangle_{\mathscr{Q}_{\mathrm{h}}}\right]$
- $\langle \lambda_{\mathrm{h}}^l - \lambda_{\mathrm{h}}^{l-1}; \nu_{\mathrm{h}}\rangle_{\mathscr{W}_{\mathrm{h}}} = -\rho_2\langle \gamma_{\mathrm{h}}^l - \nabla u_{\mathrm{h}}^l; \nu_{\mathrm{h}}\rangle_{\mathscr{W}_{\mathrm{h}}}$

5. Numerical experiments

5.1. Annular viscometer

To our knowledge, no problem set on a multidimensional polygonal domain and admitting an analytic solution can be found in the literature for viscoplastic fluids. As an alternative, we consider an axisymmetrical problem that will be treated in the following as a fully bi-dimensional one: the tangential creeping flow in a viscometer made of two coaxial cylinders. The outer cylinder is kept fixed whereas a constant angular velocity $\omega = 1$ is imposed to the inner cylinder and the fluid is supposed to stick to the apparatus boundaries, see in Fig. 4. Depending on the rheological properties of the fluid, an analytical solution can be obtained. For the Power-Law model and by extension for the Newtonian model, the tangential velocity is [4, Chapter 4, p. 239]

$$u_\theta(r) = r\omega\left[\left(\frac{R_o}{r}\right)^{2/N} - 1\right] \Big/ \left[\left(\frac{R_o}{R_i}\right)^{2/N} - 1\right]. \tag{11}$$

For fluids concerned with a yield stress, we restrict ourselves to cases where a "rigid" zone appears near the outer cylinder. Analytical solutions that provide the transition radius between the sheared and the solid zones and the tangential velocity can be obtained at least for certain values of the exponent N. For a Bingham fluid ([4, Chapter 4, p. 228]), the transition radius R_l is solution of

$$\left(\frac{R_l}{R_i}\right)^2 - 2\ln\left(\frac{R_l}{R_i}\right) - \left(\frac{2\sqrt{2}\mu\omega}{\tau_Y} + 1\right) = 0$$

and, in the sheared zone, the tangential velocity is

$$u_\theta(r) = r\frac{\sqrt{2}\tau_Y}{4\mu}\left(\left(\frac{R_l}{r}\right)^2 - 2\ln\left(\frac{R_l}{r}\right) - 1\right). \tag{12}$$

For a pseudoplastic Herschel–Bulkley fluid of exponent $N = 0.5$, the transition radius R_l is solution of:

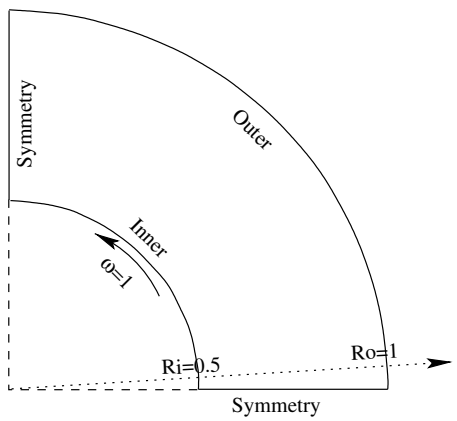

Fig. 4. Principle diagram.

$$\left(\frac{R_l}{R_i}\right)^4 - 4\left(\frac{R_l}{R_i}\right)^2 + 4\ln\left(\frac{R_l}{R_i}\right) - \left(\frac{8\sqrt{2}\mu^2\omega}{\tau_Y^2} - 3\right) = 0$$

and, in the sheared zone, the tangential velocity reads

$$u_\theta(r) = r\frac{\sqrt{2}\tau_Y^2}{4\mu^2}\left(\frac{3}{4} + \frac{R_l^4}{4r^4} - \frac{R_l^2}{r^2} + \ln\left(\frac{R_l}{r}\right)\right). \tag{13}$$

The aim of this numerical experiment is twofold as both the methodologies to take into account the constitutive law and to approximate the system of equations on a domain immersed on a fixed computational grid are tested. Two series of finer and finer unstructured meshes have been built using a Delaunay–Voronoï automatic meshing process (EMC2 pre-processor [31]). Meshes of the first series are fitted on the physical domain (Fig. 4) whereas the other ones are built on a larger geometrical domain. The coarsest meshes of the two series are drawn on Fig. 5. Computations made on the grid fitted to the physical domain will be referred as "fitted" computations by opposite to those made with a "free surface". Finer meshes are obtained by using twice the number of vertices on each line segment or each arc of the domain boundaries. Analytical solutions are represented by lines on Fig. 6 for the rheological parameters of Table 5. We have added as symbols the computed nodal values obtained with a coarse grid fitted to the physical domain. Those values are in good agreement with analytical solutions what will be confirmed by the following error bound analysis. For the "free surface" computations, an appropriate boundary condition must be added at the free surface. If the constitutive law is sufficiently regular, stresses are defined everywhere and analytical ones can be used to define a Neumann boundary condition at the outer cylinder that is to say for the Power-Law model:

$$\sigma.\vec{n} = 2\mu\left[\frac{\omega}{N\left(\left(\frac{R_o}{R_i}\right)^{2/N} - 1\right)}\right]^N \vec{t},$$

where $\vec{n}$ and $\vec{t}$ denote the normal and the tangent to the free surface, respectively. On the opposite, for the fluids concerned with a yield stress, as we are interested in cases where a "rigid" zone appears near the outer cylinder, the velocity field must be constrained to vanish on the free surface by penalization.

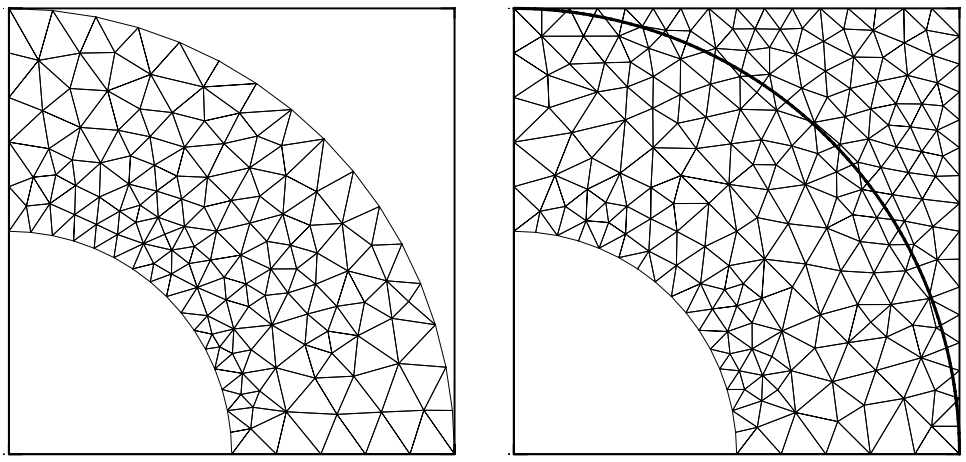

Fig. 5. Coarsest meshes for the fitted to physical domain series and the series based on a larger geometrical domain.

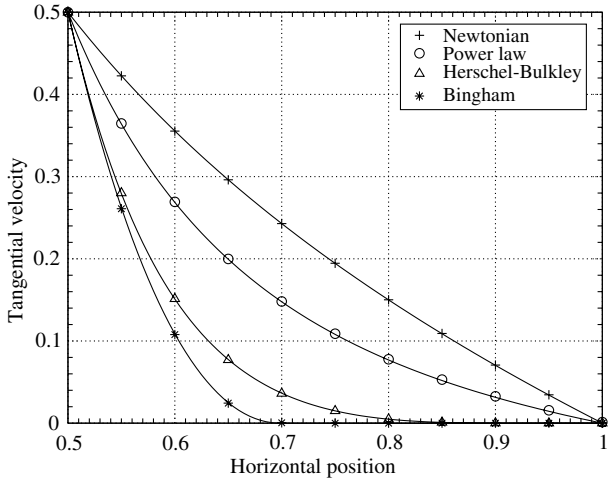

Fig. 6. Tangential velocity at $(z = 0, r \in [0.5; 1])$, plain lines for the analytical solutions (11)–(13) and symbols for the corresponding computed nodal values.

Table 5
Rheological parameters for the viscometer benchmark

Newtonian	Power-Law	Bingham	Herschel–Bulkley
$\mu = 1$	$N = 0.5$, $\mu = 0.08$	$\tau_Y = 10$, $\mu = 1$	$N = 0.5$, $\tau_Y = 0.12$, $\mu = 0.0672$

The term

$$\frac{1}{\epsilon}\int_{\partial\Omega_N} ||u_h||^2 \mathrm{d}\partial\Omega, \quad \epsilon \ll 1,$$

where $\partial\Omega_N$ denotes the free surface, is indeed added to the saddle point problem (9). The remaining of this section is aimed at the validation of both methodologies by the convergence analysis of the relative L2-norm and H1-norm of the error:

$$\frac{||u_e - u_h||_0}{||u_e||_0}, \quad \text{where} \quad ||u_e - u_h||_0^2 = \int_{\Omega_f} ||u_e - u_h||^2 \,\mathrm{d}\Omega \,,$$
$$\frac{||u_e - u_h||_1}{||u_e||_1}, \quad \text{where} \quad ||u_e - u_h||_1^2 = ||u_e - u_h||_0^2 + \int_{\Omega_f} ||\nabla(u_e - u_h)||^2 \,\mathrm{d}\Omega \,,$$

where u_e denotes the analytical solution. The results for the computations performed with the two series of ''fitted'' and with ''free surface'' meshes are provided on Fig. 7 for the Newtonian and the power-law model (Neumann boundary condition) and on Fig. 8 for the Bingham and the Herschel–Bulkley model (outer boundary velocity constrained by penalty). The results obtained with the two series of meshes are similar which provides a validation of the methodology used to approximate the system of equations on a domain immersed in a fixed computational grid. Moreover the convergence rates we obtained for the Newtonian model are those that was expected. For the Bingham model, we have proved in [22] that with the Brezzi–Pitkäranta stabilization one retrieves an error bound estimate of the same order than that one Han and Reddy obtained for space discretizations that fulfills the BB condition, that is to say

$$||u_e - u_h||_1 \leqslant C\sqrt{h},$$

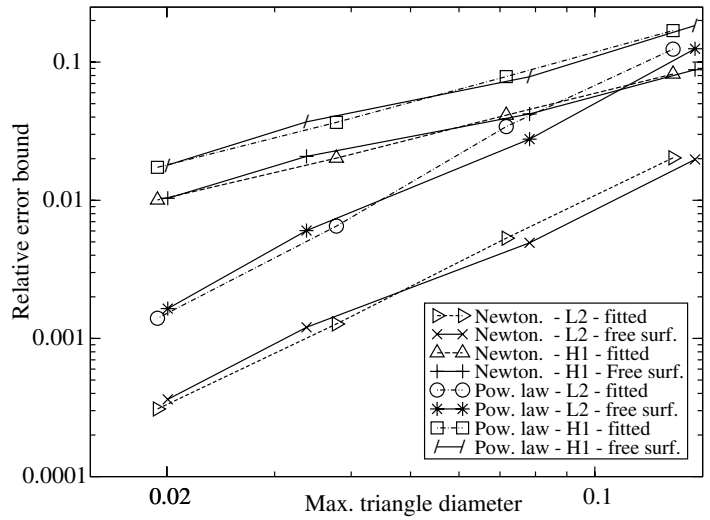

Fig. 7. Errors for the Newtonian (Newt.) and the Power-Law (Pow. law) models and for both the "fitted" (dashed lines) and the "free surface" (solid lines) computations.

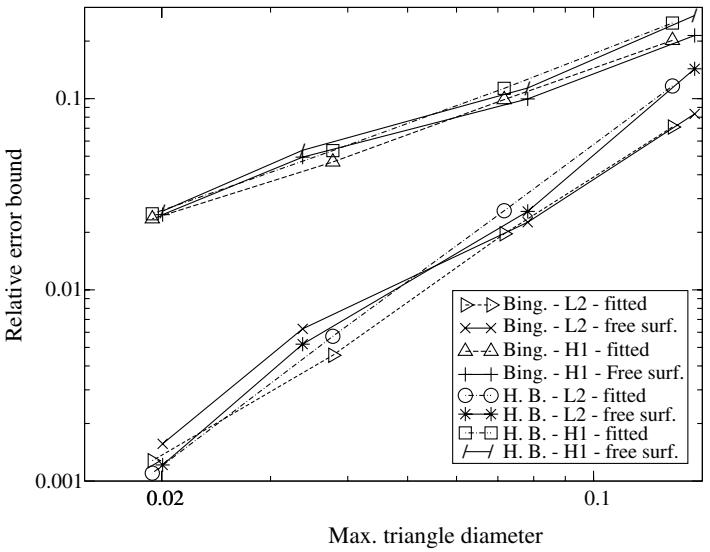

Fig. 8. Errors for the Bingham (Bing.) and the Herschel–Bulkley (H.-B.) models and for both the "fitted" (dashed lines) and the "free surface" (solid lines) computations.

where C is a positive constant independent on the mesh parameter h. But one can also found in [22] an extended analysis of this viscometer benchmark for the Bingham model that shows that, due to a higher regularity of the analytical solution in this specific case, convergence rates of higher order can be expected and are reached

$$||u_e - u_h||_1 \leqslant Ch\sqrt{|\log(h)|}.$$

As can be observed in the results of Fig. 8, those improved convergence rates are again obtained for all tested constitutive laws. In addition, a second order convergence rate is observed in L2-norm.

As a last verification test, we have made a convergence study with a series of meshes obtained by cutting successively the triangles of the original coarse mesh fitted to the physical domain (left mesh of Fig. 5) into four triangles of equal size. As expected in this case we have checked that the above-mentioned improved convergence rates are lost due to the well-known "variational crime", see for example [5]. The error is indeed never less than 3×10^{-3} and 1.4×10^{-2} for the relative L2-norm and for the relative H1-norm, respectively.

More results concerning the fictitious degrees of freedom method applied to some elliptic PDEs posed on domain with immersed boundary can be found in [21].

Table 6
Rheological parameters for the models of Table 2

	Newtonian	Power-Law	Bingham	Herschel–Bulkley pseudoplastic	Herschel–Bulkley dilatant
μ (N m^{-2} s)	0.5	1.74	0.01	0.25	0.0025
τ_Y (Nm^2)	0	0	5	3.5	4.9
N	1	0.15	1	0.4	1.5

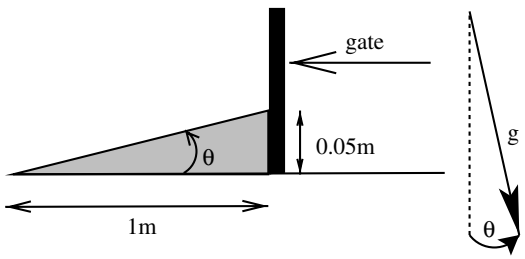

Fig. 9. Principle diagram.

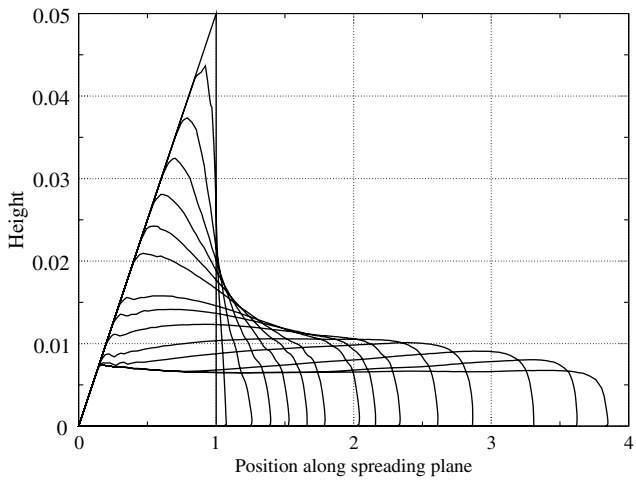

Fig. 10. Successive profiles of the free surface at times 0, 0.1, 0.3, 0.5, 0.7, 0.9, 1.1, 1.5, 1.7, 2, 2.5, 3, 4, 5, 10 s for the Bingham fluid.

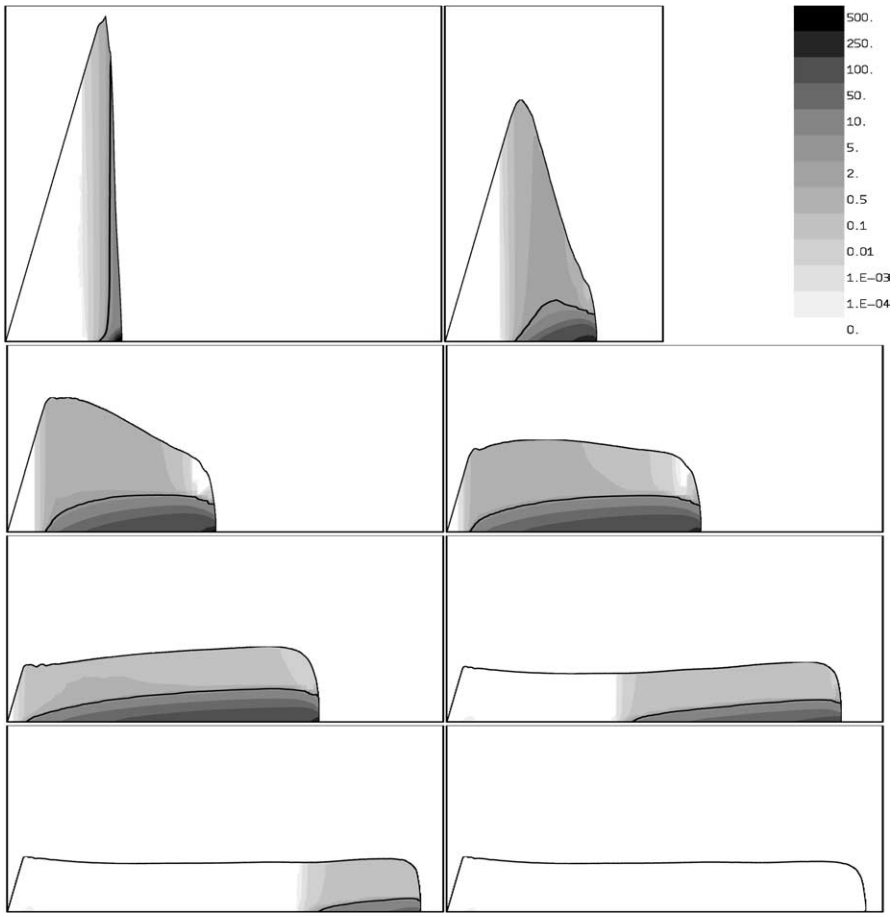

Fig. 11. Free surface profiles and shear strain rate magnitude for the Bingham fluid at times 0.1, 0.5, 1.3, 2, 3, 5, 6, 10 s (when the flow is stopped). Horizontal axis length is of 4 m whereas the vertical axis length is of 0.045 m for the first two figures and of 0.025 m for the last six ones. Sheared zones are in black to light gray gray-scales, solid zones are in white and a black line marks the separation between zones where the shear strain rate magnitude is lower or greater than 5 s^{-1}.

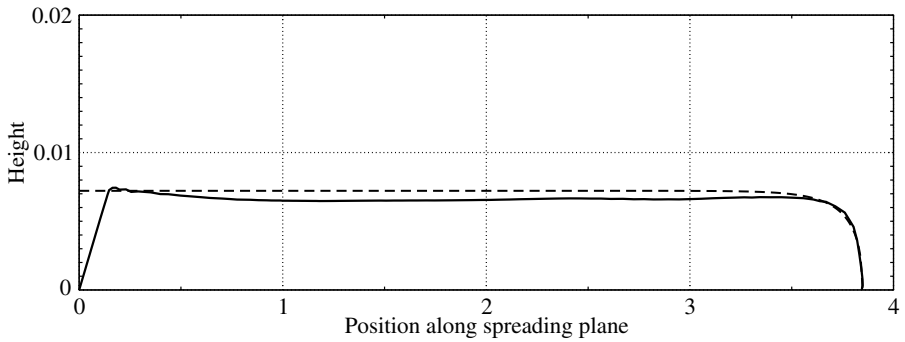

Fig. 12. Comparison of the permanent profile obtained for the Bingham fluid with an analytical one valid at the downstream front [23].

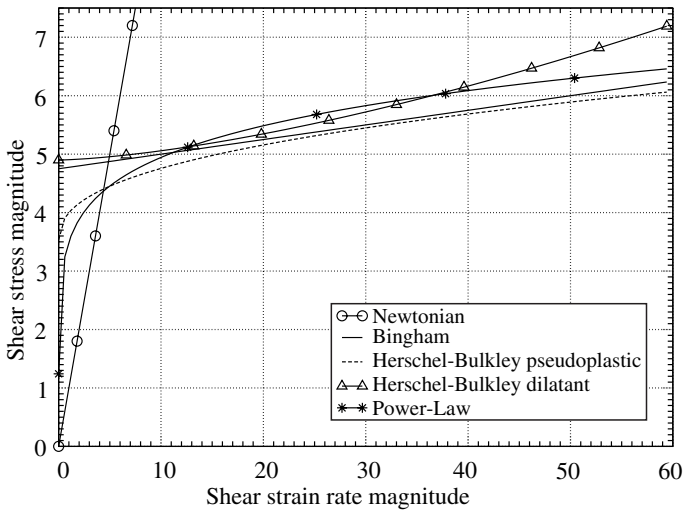

Fig. 13. Rheogram for the different models (parameters of Table 6).

5.2. Flow down a slope

The rheological properties of muds are known to exhibit a non-Newtonian behavior, in some cases accurately described by a viscoplastic model with shear-thinning [2] and flows of mud down a slope have been one of the most frequently encountered application fields for non-Newtonian fluid mechanics. The problem considered in this section is inspired from such a study [16]. This analysis, proposed by Huang and Garcia, is based on the thin-flow approximation for which the rheological properties of the fluid are modeled as a frictional term at the interface between the fluid and the plane. To reach, from the data of Huang and Garcia's computation, the "volume" rheological properties, one would need to build some correlations between the constitutive relation and the interfacial friction strength, for instance by a series of numerical experiments. This work is out of the scope of the present study and we have restricted ourselves

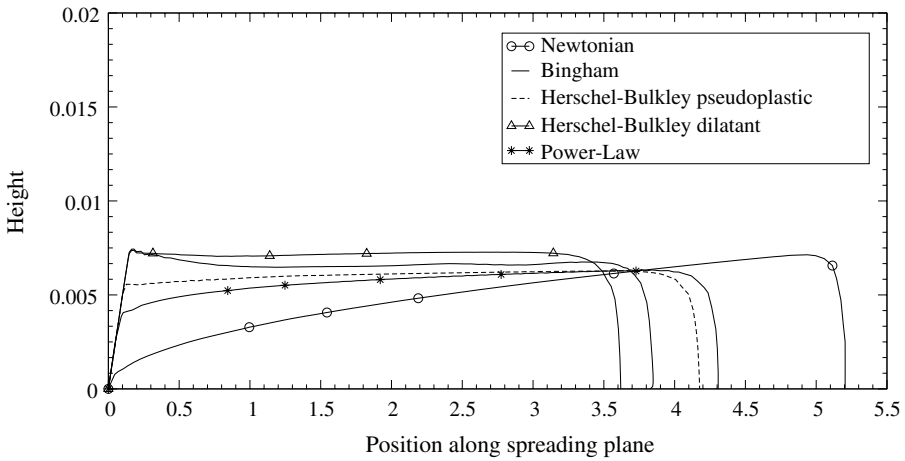

Fig. 14. Profiles obtained at 100 s for the different rheological models.

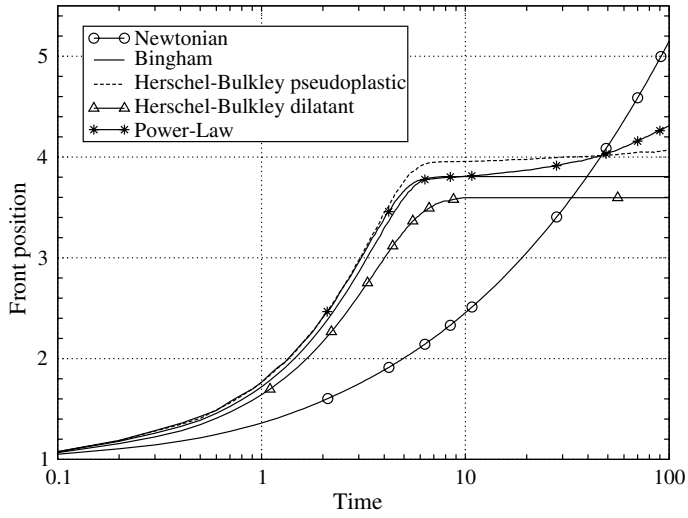

Fig. 15. Front position evolution for the different rheological models.

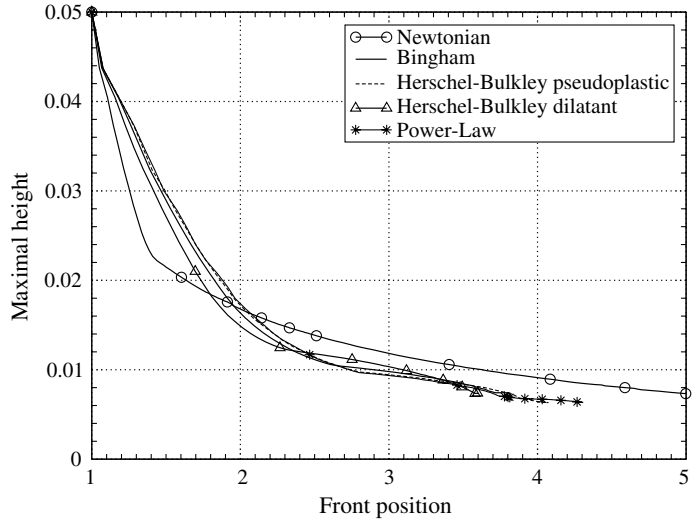

Fig. 16. Evolution of the maximal height versus front position.

to a qualitative analysis. All rheological properties have then been chosen to fulfill the two following requirements: being in a range of magnitude compatible with the rheological properties of muds and, above all, allowing to make comparisons between the different rheological models, see Table 6 and Fig. 13. All fluids are assumed to have a density of 1000 kg/m^3. The principle diagram is drawn in Fig. 9. An amount of fluid is deposited on an inclined plane (angle $\theta = \tan^{-1}(0.05)$ – the aspect ratio is thus large) and is contained by a gate that is instantaneously removed at initial time. The fluid is assumed to stick to the spreading plane. The computation duration is of 100 s and an adaptive time step procedure is adopted with an initial time step of 10^{-2} s. Calculation are performed with a computational grid made of 14,000 triangles and refined in the vicinity of the initial fluid front.

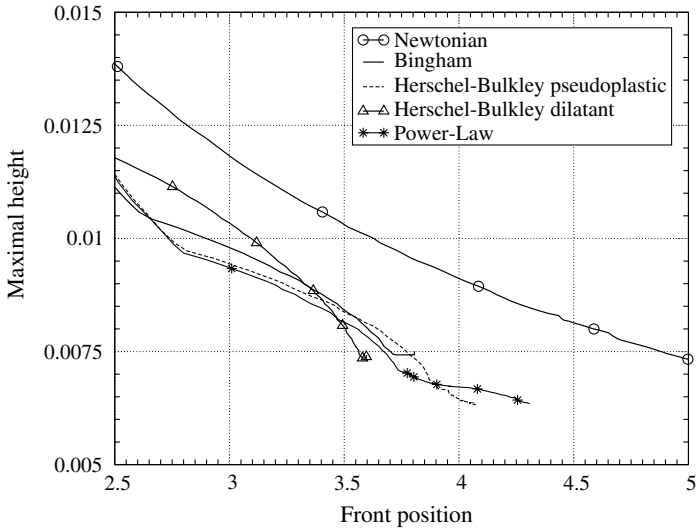

Fig. 17. Same as Fig. 16 with zoom on the last front positions.

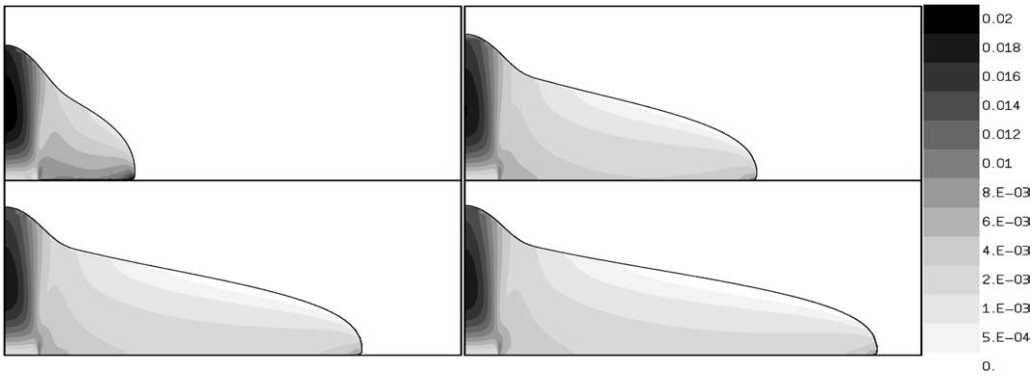

Fig. 18. Free surface profiles and shear strain rate magnitude for the Newtonian fluid (Bi = 0) at times 10^3, 5×10^3, 7.5×10^3 and 10^4. The radius axis and the vertical axis lengths correspond to 2 and 0.2 unit-lengths, respectively. Sheared zones are in black to light gray gray-scales.

We first present extensively the results we obtain for the Bingham fluid. The evolution of the free surface profiles from the initial fluid location to the time the fluid comes to rest is drawn in Fig. 10. The flow is essentially split into two stages, first a fast sinking of the fluid top followed by a slower viscous spreading until it stops by $t = 10$ s. Maps of the shear strain rate magnitude at different times are drawn in Fig. 11. We observe a decomposition of the flow in essentially three zones:

- a first zone located near the spreading plane and in the downstream part of the flow where the shear strain rate magnitude is very large (895 s^{-1} at 0.5 s),
- an upstream unsheared zone, which becomes smaller and smaller in the beginning of the transient but never disappears, before growing up to cover the whole flow at the end of the spreading,
- between those last two zones, an intermediate one where the fluid is sheared but with a shear strain rate magnitude considerably lower than near the spreading plane (lower than 5 s^{-1}, i.e., about two-hundred times lower than the maximal shear strain rate magnitude).

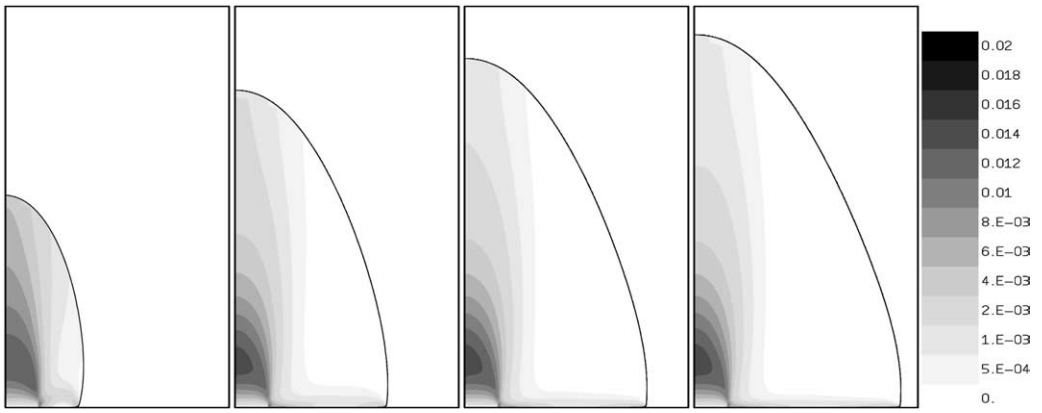

Fig. 19. Free surface profiles and shear strain rate magnitude for the Bingham fluid (Bi = 0.1) at times 10^3, 5×10^3, 7.5×10^3 and 10^4. The radius axis and the vertical axis lengths correspond to 1 and 0.55 unit-lengths, respectively. Sheared zones are in black to light gray gray-scales.

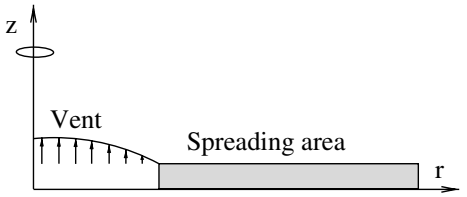

Fig. 20. Principle diagram.

This decomposition remains valid from the onset of the flow until the fluid comes at rest. The picture obtained here then slightly differs from the scheme used in simulations of slow spreading of a viscoplastic fluid quoted in the literature, which, to our knowledge have all been made under the thin flow assumption combined with the so-called two-layers hypothesis: at each "horizontal" location, the flow is supposed to be split into an unsheared upper layer and a sheared lower one. However, no any significant difference is to be expected in the global flow behavior as long as the apparent viscosity within the intermediate layer remains large.

One may note that no smoothing of the free surface is processed. Together with the sharp aspect of the initial fluid domain, this explains the small oscillations that can be observed on the profile of the free surface during the convection-dominated stage of the flow (see Fig. 10) whereas they have disappeared after the diffusion-dominated stage (see Figs. 10 and 12). Mass conservation is a key point for those free surface problems, a mass lost is indeed observed during the convection-dominated stage of the flow but remains limited as the cumulative mass loss is equal to -0.371% of the original mass when the flow stops. We have made a comparison of the permanent profile we obtain when the flow stops with the analytical profile known to be valid in the downstream part of the fluid [23], where the fluid height h is given as a function of the abscissa along the plane x by

$$\tan(\theta)(x - x_{\mathrm{f}}) = \frac{h}{\bar{h}} + \ln\left(1 - \frac{h}{\bar{h}}\right),$$

where x_{f} is the downstream front position and

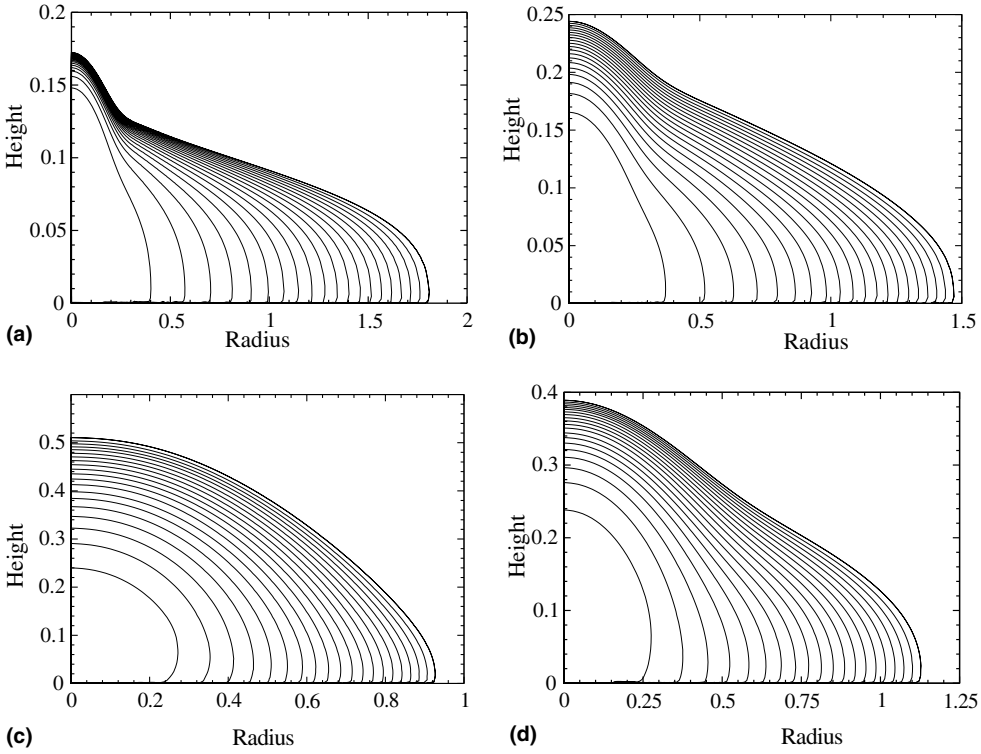

Fig. 21. Evolution of the free surface profiles from time 5×10^2 to time 1×10^4 by step of 5×10^2 time units for various rheological properties. (a) Newtonian (Bi = 0.), (b) Bingham (Bi = 0.01), (c) Bingham (Bi = 0.1), (d) Herschel–Bulkley (Bi = 0.01, $N = 0.5$).

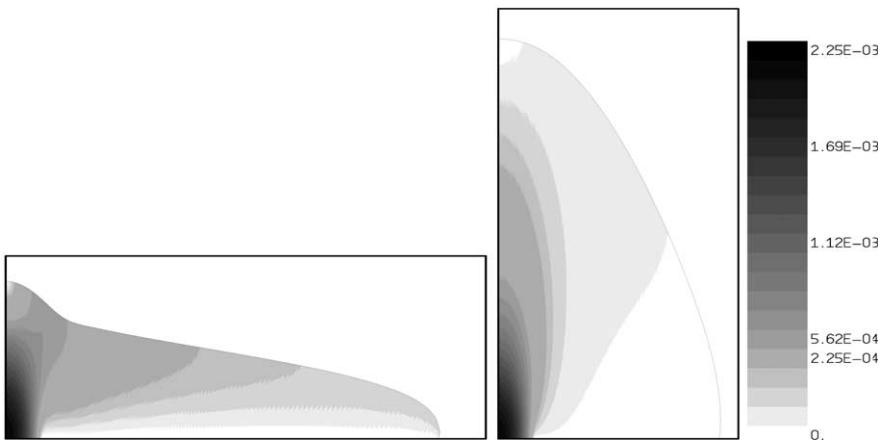

Fig. 22. Velocity magnitude maps for the Newtonian fluid and for the Bingham fluid at time 1×10^4. The axis lengths are, respectively, the same as in Figs. 18 and 19.

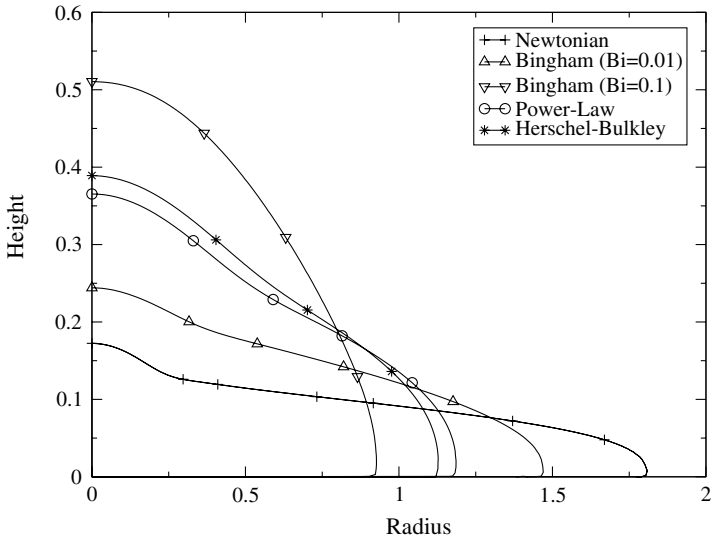

Fig. 23. Profiles after 10^4 unit-times for the different rheological properties.

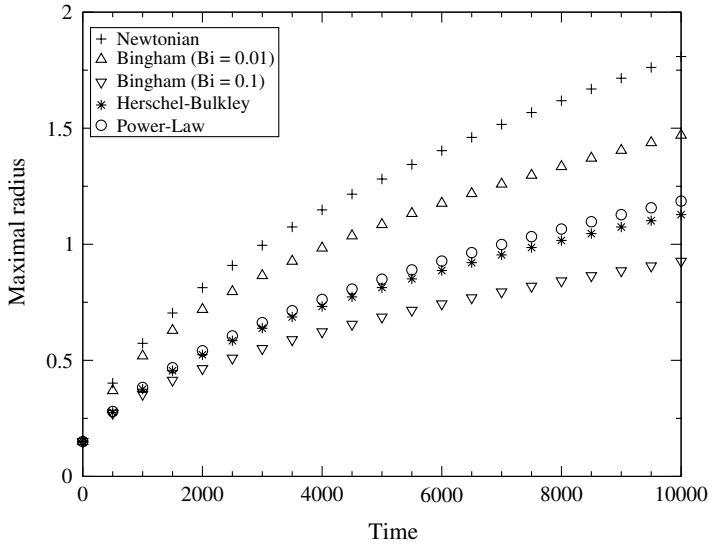

Fig. 24. Dome radius evolution for the different rheological properties.

$$\bar{h} = \frac{\rho g}{\tau_Y} \sin(\theta)$$

is the expression of the theoretical minimal height beyond which an infinite uniform layer of viscoplastic fluid deposited on an inclined plane starts to flow without any external perturbation. Profiles are in good agreement in the downstream zone as checked in Fig. 12, the observed slight differences being due to history effects.

Final part of this analysis is devoted to the comparison of spreading evolutions obtained for various rheological models presented in Table 6 and Fig. 13. The free-surface profiles at 100 s for all rheological models are drawn in Fig. 14. As can be observed in Fig. 15, the Bingham and the dilatant Herschel–Bulkley rheological fluids came to rest before 10 s. The sharp upstream zone is similar for those two fluids. A larger part of this upstream zone has sunk down for the Herschel–Bulkley pseudoplastic fluid that is almost stopping at 100 s and for the Power-Law fluid whereas it is quickly spread for the Newtonian fluid. The time evolution of the front position and the evolution of the maximal height versus the front position are shown in Figs. 15–17. Those results are qualitatively in agreement with the results of Huang and Garcia [16].

5.3. Growing of isothermal lava domes

We are now interested in a problem that has been defined by Balmforth et al. [1], namely the simulation of the growth of an isothermal quasi-Newtonian dome, which can be considered as an idealized representation of lava domes eruption above the conduit that links the magma chamber to the atmosphere (see [15,33] for more details about the physical background).

The principle diagram is drawn in Fig. 20. The non-dimensionalization of the governing equations and of the rheological model are proposed in [1] and we will use the same notations. The entrance flow on the vent of radius 0.15 unit-length is assumed to keep the following constant with time value:

$$u_{\text{vent}}.n = 2.25 \times 10^{-3} \ * \left(1. - \left(\frac{r}{0.15}\right)^2\right).$$

Moreover we have assumed that, at initial time, the fluid is at rest at the location reached after 0.25 time unit of pure convection, leading to the following initial shape for the free surface:

$$\begin{cases} r \in [0, 0.15], & h = 5.625 \times 10^{-4} \ * \left(1. - \left(\dfrac{r}{0.15}\right)^2\right), \\ r > 0.15, & h = 0. \end{cases}$$

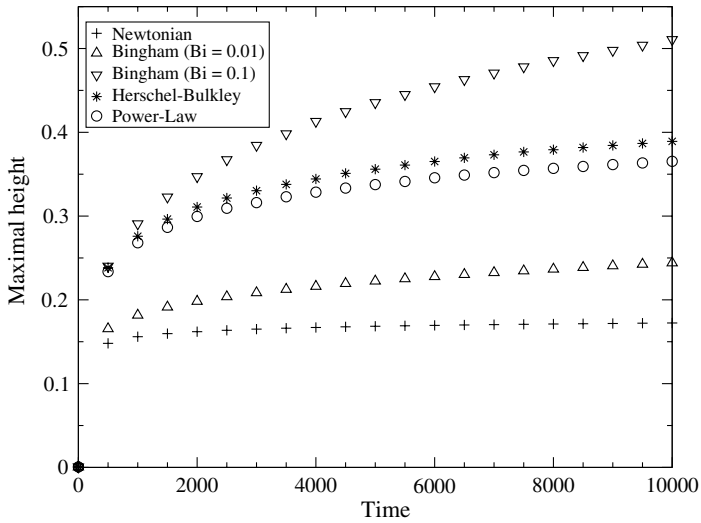

Fig. 25. Maximal height evolution for the different rheological properties.

The computation duration is of 10^4 unit-times with a constant time step of 2 unit-times (saving for post processing are made each 5×10^2 unit-times). Calculation are performed with a computational grid made of 21,000 triangles and refined in the vicinity of the vent. Maps of the shear strain rate magnitude for various times are drawn on Fig. 18 for a Newtonian behavior and on Fig. 19 for a Bingham behavior ($\mathrm{Bi} = 0.1$). Except for the zone located up to the vent, the sheared zones are almost uniformly distributed for the Newtonian fluid whereas, for the Bingham fluid, the most sheared zones are concentrated near the spreading area.

Finally, we finish this study by a comparison of the domes evolutions for various fluids of different rheological properties, the Newtonian fluid, two Bingham fluids ($\mathrm{Bi} = 0.01$ and $\mathrm{Bi} = 0.1$) and, to illustrate the yield stress and shear-thinning effects, a Herschel–Bulkley fluid ($\mathrm{Bi} = 0.01$ and $N = 0.5$) and a Power-Law fluid ($N = 0.5$). Results are shown in Figs. 21–25.

Acknowledgements

The authors thank their colleagues of the development teams of the software component library PELICANS and of the finite element code CROCO for their constant help and useful comments on this paper.

References

[1] N.J. Balmforth, A.S. Burbidge, R.V. Craster, J. Salzig, A. Shen, Visco-plastic models of isothermal lava domes, J. Fluid Mech. 403 (2000) 37–65.
[2] N.J. Balmforth, A. Provenzale (Eds.), Geomorphological Fluid Mechanics, Springer, Berlin, 2001, number 582 in Lecture Notes Phys.
[3] M. Bercovier, O. Pironneau, V. Sastri, Finite elements and characteristics for some parabolic-hyperbolic problems, Appl. Math. Model 7 (1983) 89–96.
[4] R.B. Bird, R.C. Armstrong, O. Hassager, Dynamics of Polymeric Liquids – Vol. 1 Fluid Mechanics, second ed., Wiley-Interscience, New York, 1987.
[5] S.C. Brenner, L.R. Scott, The Mathematical Theory of Finite Element Analysis, Volume 15 of Texts in Applied Mathematics, Springer-Verlag, Berlin, 1991.
[6] F. Brezzi, J. Pitkäranta, On the stabilization of finite element approximations of the Stokes equations, in: W. Hackbusch (Ed.), Efficient Solution of Elliptic Systems, Volume 10 of Notes Numerical Fluid Mechanics, Vieweg, 1984, pp. 11–19.
[7] P.G. Ciarlet, Basic error estimates for elliptic problems, in: P.G. Ciarlet, J.L. Lions (Eds.), Handbook of Numerical Analysis Volume II: Finite Elements Methods, North-Holland, New York, 1991.
[8] E.J. Dean, R. Glowinski, Operator-splitting methods for the simulation of Bingham visco-plastic flow, Chin. Ann. Math. Ser. B 23B (2002) 187–204.
[9] G. Duvaut, J.L. Lions, Inequalities in Mechanics and Physics, Springer-Verlag, Berlin, 1976.
[10] A. Fortin, D. Côté, P.A. Tanguy, On the imposition of friction boundary conditions for the numerical simulation of Bingham fluid flows, Comput. Meth. Appl. Mech. Eng. 88 (1991) 97–109.
[11] M. Fortin, R. Glowinski, Méthodes de Lagrangien Augmenté. Application à la résolution numérique de problèmes aux limites, Dunod-Bordas, Paris, 1982.
[12] P. Germain, Q.S. Nguyen, P. Suquet, Continuum thermodynamics, J. Appl. Mech. 3 (1983) 1010–1020.
[13] R. Glowinski, Numerical Methods for Nonlinear Variational Problems, Springer-Verlag, New York, 1984.
[14] R. Glowinski, O. Pironneau, Finite element methods for Navier–Stokes equations, Annu. Rev. Fluid Mech. 24 (1992) 167–204.
[15] R.W. Griffiths, The dynamics of lava flows, Annu. Rev. Fluid Mech. 32 (2000) 477–518.
[16] Xin Huang, Marcelo H. García, A Herschel–Bulkley model for mud flow down a slope, J. Fluid Mech. 374 (1998) 305–333.
[17] D. Jacqmin, Calculation of two-phase Navier–Stokes flows using phase-field modeling, J. Comput. Phys. 155 (1999) 96–127.
[18] D. Jamet, O. Legaigue, N. Coutris, J.M. Delhaye, The second gradient method for the direct numerical simulation of liquid-vapor flows with phase-change, J. Comput. Phys. 169 (2001) 624–651.
[19] J.H. Jeong, D.Y. Yang, Finite element analysis of transient fluid flow with free surface using VOF (Volume-Of-Fluid) method and adaptative grid, Inter. J. Numer. Method Fluid 26 (1998) 1127–1154.
[20] D.B. Kothe, D. Juric, K. Lam, B. Lally, Numerical recipes for mold filling simulation, in: Eighth International Conference on Modeling of Casting, Welding, and Advanced Solidification Processes, San Diego, CA, 1998.

[21] J.-C. Latché, Fictious node method for free surface flows, submitted for publication.
[22] J.-C. Latché, D. Vola, Analysis of the Brezzi–Pitkaranta stabilized Galerkin scheme for creeping flows of Bingham fluids, SIAM J. Numer. Anal. (in press).
[23] K.F. Liu, C.C. Mei, Slow spreading of a sheet of Bingham fluid on a inclined plane, J. Fluid Mech. 207 (1989) 505–529.
[24] J.M. Martinez, Qi. Linqun, Inexact Newton methods for solving nonsmooth equations, J. Comput. Appl. Math. 60 (1–2) (1995) 127–145.
[25] B.D. Michel, B. Piar, F. Babik, J.-C. Latché, G. Guillard, C. De Pascale, Synthesis of the validation of the CROCO V1 spreading code, in: OECD Workshop on Ex-Vessel Debris Coolability, Karlsruhe, Germany, November 15–18, 1999.
[26] S. Osher, R.P. Fedkiw, Level set methods: an overview and some recent results, J. Comput. Phys. 169 (2001) 463–502.
[27] D. Perić, S. Slijepčević, Computational modelling of viscoplastic fluids based on a stabilized finite element method, Eng. Comput. 18 (3/4) (2001) 577–591.
[28] B. Piar, B.D. Michel, F. Babik, J.-C. Latché, G. Guillard, J.-M. Ruggiéri, CROCO: a computer code for corium spreading, in: Ninth International Topical Meeting on Nuclear Reactor Thermal Hydraulics (NURETH-9), San Francisco, CA, October 3–8, 1999.
[29] A. Prosperetti, G. Tryggvason, Appendix 3: report of study group on computational physics, Inter. J. Multiphase Flow 29 (7) (2003) 1089–1099.
[30] Nicolas Roquet, Pierre Saramito, An adaptive finite element method for Bingham fluid flows around a cylinder, Comput. Methods Appl. Mech. Eng. 192 (31–32) (2003) 3317–3341.
[31] Eric Saltel, Frédéric Hecht, EMC2 un logiciel d'édition de maillages et de contours bidimensionnels, Technical Report 118, INRIA, October 1995. Available from <http://www-rocq1.inria.fr/gamma/cdrom/www/emc2/eng.htm>.
[32] J.A. Sethian, Level Set Methods. Cambridge Monographs on Applied and Computational Mathematics, Cambridge University Press, Cambridge, 1998.
[33] Mark V. Stasiuk, Claude Jaupart, Lava flow shapes and dimensions as reflections of magma system conditions, J. Volcanol. Geotherm. Res. 78 (1997) 31–50.
[34] G.T. Toussaint, Efficient triangulation of simple polygons, Visual Computer 7 (1991) 280–295.
[35] D. Vola, L. Boscardin, J.-C. Latché, Laminar unsteady flows of Bingham fluids: a numerical strategy and some benchmark results, J. Comput. Phys. 187 (2) (2003) 441–456.